LAF | https://doi.org/10.15302/J-LAF-2026-0038
Volume 14 / Issue 5 / 260038 / 2026
Received Date | 2025-10-18 Accepted Date | 2026-06-11
© Higher Education Press 2026

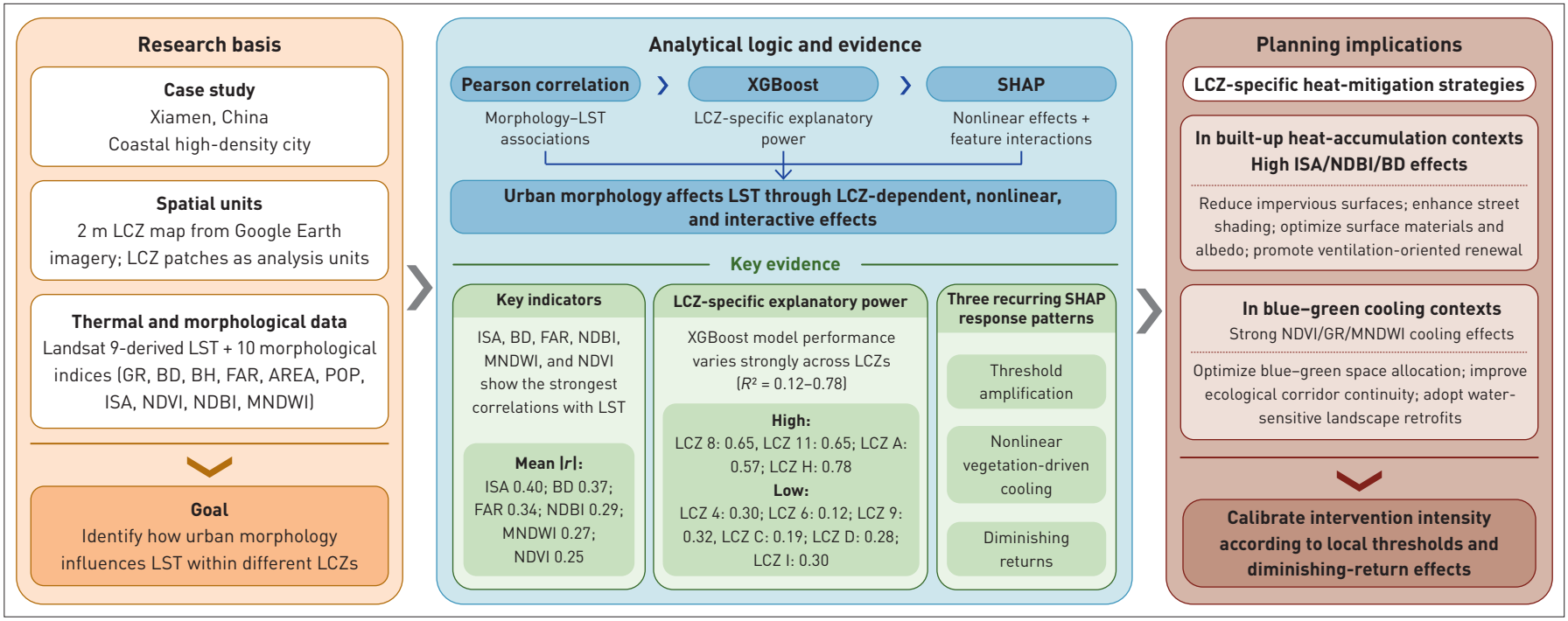
The Impact of Urban Spatial Morphology on Local Climate Zone Surface Temperature

Xiang LIU[1], Hongfei YU[2,*], Xiaowei LU[3], Juan YU[1], Ruhong XIN[4]

1 School of Civil Engineering and Architecture, University of Jinan, Jinan 250022, China
2 China State Construction Eighth Engineering Division First Construction Co., Ltd., Jinan 250014, China
3 Shanghai Municipal Engineering Design and Research Institute (Group) Co., Ltd., Shanghai 200092, China
4 College of Horticulture and Landscape Architecture, Southwest University, Chongqing 400715, China

*CORRESPONDING AUTHOR
Address: 5th Floor, Tower C, Sanqing Century Fortune Centre, Lixia District, Jinan 250014, China
Email: yuhongfei.young@163.com

GRAPHICAL ABSTRACT



ABSTRACT

Global warming has led to an increasing frequency of extreme heat events, worsening urban thermal environments. Precise regulation of urban spatial morphology is an effective approach to mitigating urban heat stress. The Local Climate Zone (LCZ) framework provides a robust framework for linking urban form with the urban thermal environment. Taking Xiamen as a case study, this research applied a convolutional neural network to generate a high-resolution LCZ map and selected 10 spatial morphological indices, including building density, floor area ratio, and greening ratio, to analyze their relationships with land surface temperature (LST). Correlation analysis, XGBoost, and SHAP were employed to investigate these relationships. The results reveal that: 1) impervious surface area, building density, floor area ratio, normalized difference built-up index, normalized difference vegetation index, and modified normalized difference water index exhibit the strongest correlations with LST across LCZs; 2) the XGBoost regression results indicate that the explanatory power of the 10 indices for LST varies across LCZs, ranging from 0.12 to 0.78; and 3) SHAP analysis provides a robust interpretation of the XGBoost results, with the interactions among the 10 indices broadly characterized by three patterns:

threshold-amplification, nonlinear cooling, and diminishing returns. The results offer a scientific basis for refined urban planning and climate-adaptive design and contribute to enhancing urban climate resilience.

KEYWORDS

Local Climate Zone; Urban Spatial Morphology; Land Surface Temperature; Spatial Heterogeneity; XGBoost–SHAP

HIGHLIGHTS

- Urban morphology exerts heterogeneous effects on LST across LCZ classes
- XGBoost–SHAP reveals nonlinear and interactive thermal responses
- Identifies nonlinear response patterns: threshold amplification, nonlinear cooling, and diminishing returns
- LCZ-specific regulation enables targeted and efficient urban heat mitigation

RESEARCH FUNDS

- Key Project of the Shandong Provincial Soft Science Research Program (No. 2026RZB0108)
- Research Project for Newly Recruited Talents (Science and Technology), University of Jinan (No. XBS2510)

1 Introduction

Global climate warming has become a critical factor constraining human survival and development over the past century[1–3]. Data released by the United Nations Climate Action initiative indicate that the global mean temperature has risen by 1.1 °C since the Industrial Revolution[4]. During this period, the disorderly expansion of Chinese cities amid rapid urbanization has significantly deteriorated urban thermal environments[5–7]. At present, most cities in China have entered the latter stage of urbanization, with the focus of urban development shifting from quantitative expansion to qualitative improvement[8]. Nevertheless, the intensification of the urban heat island (UHI) effect and threats to ecological security are becoming increasingly prominent. Against this backdrop, mitigating thermal stress through the optimization of urban spatial morphology has become a central issue in interdisciplinary research on architecture, urban studies, and climate adaptation[9–12].

In recent years, numerous studies worldwide have investigated the driving mechanisms of land surface temperature (LST) and the UHI effect. A general consensus has emerged that factors such as greening ratio, impervious surface area, and building morphology exert significant impacts on the urban thermal environment[13–17]. For instance, Xuefan Zhou and Hong Chen pointed out that land-use changes driven by rapid urbanization have intensified the UHI effect globally[18]; Jun Yang et al. revealed the complex roles of different spatial morphological factors in LST using multi-source datasets[19]. However, most existing studies still focus on the linear effects of single factors, with insufficient attention to synergistic interactions and spatial non-stationarity, which limits their ability to provide transferable evidence for localized governance. At present, there is still a lack of an effective land-use classification framework that can directly and systematically link LST with urban spatial morphology.

The Local Climate Zone (LCZ) classification, as an emerging system characterizing both urban morphology and climatic features, offers a systematic framework for analyzing the spatial differentiation of thermal environments[9,20]. By delineating urban areas with similar surface cover, building configuration, and microclimatic characteristics, LCZs can effectively capture spatial heterogeneity in urban thermal environments[21–22]. Nevertheless, existing research often emphasizes the thermal impacts of single morphological indicators (e.g., greening ratio, building density)[23], while overlooking the synergistic roles of multiple spatial factors. In addition, traditional statistical models struggle to capture the spatial non-stationarity of thermal effects[18–19], leading to planning strategies that lack precision and adaptability.

Globally, existing studies have continuously explored the application of LCZs across diverse climatic zones and urban development stages, aiming to reveal both universal patterns and local variations. For instance, Kevin Ka-Lun Lau et al. revealed that thermal comfort in Hong Kong, China is strongly associated with LCZ classes[20]; Zahra Parvar et al. demonstrated that both 2D and 3D morphological characteristics significantly influence the thermal environment in Tehran, Iran[21]; Nada Badaro-Saliba et al. highlighted the effectiveness of the LCZ framework in assessing UHI intensity in the complex urban fabric of Beirut[22]. While these studies provide valuable references for urban heat governance, comprehensive analyses of coastal high-density cities remain scarce, particularly empirical studies that integrate

architectural, ecological, and demographic dimensions. Therefore, further research is needed to investigate the combined effects of multidimensional spatial morphological factors on LST in LCZs in coastal high-density cities.

To address the aforementioned research gap, this study aims to: 1) quantify the effects of spatial morphology on LST across LCZs and investigate the interactions among spatial morphological indices; 2)provide theoretical support for differentiated and precise thermal environment governance, advancing the transition of urban development from extensive development to precise regulation.

2 Data and Methods

2.1 Study Area

Xiamen, a sub-provincial city under the jurisdiction of Fujian Province, China, is functioning as a major port and a renowned tourist destination[24]. The city covers a total area of 1,912 km², with a current permanent population of approximately 5.18 million, which is projected to reach 7.3 million by 2035[7]. Xiamen has a subtropical monsoon climate, with a mean annual temperature of about 20.9 °C[25]. The city's elevation ranges from 0 to 1,149 m, with relatively flat terrain along the southeastern coastal zone, where the majority of the built-up area is concentrated.

As one of China's key economic growth poles, Xiamen also ranks among the most densely populated regions in the country[7]. However, the city's rapid urbanization has resulted in the widespread replacement of natural surfaces by impervious materials such as buildings and roads. This transformation has disrupted natural drainage systems and weakened thermal regulation functions, thereby exacerbating increases in LST[26–27], especially during the hot summer season[28]. Furthermore, the city's diverse architectural styles and complex urban layout exert significant impacts on LST. Therefore, as a representative coastal city, Xiamen provides an ideal case for examining urban thermal environments, LCZ classification, and the coupled relationships between them.

2.2 Research Framework

The overall research framework of this study is designed to systematically examine the coupled relationship between urban spatial morphology and LST in LCZs in Xiamen. The framework integrates multi-source data, spatial morphological indices, and statistical modeling to achieve a comprehensive analysis.

First, the LCZ map of Xiamen is generated, and the LCZ patch boundaries are used as the basic spatial units for subsequent analysis. Second, the LST map of Xiamen is retrieved using the thermal infrared band of Landsat 9 imagery. Multiple data sources are then integrated to derive a multidimensional set of spatial morphological indices representing building form, biophysical conditions, and patch-level characteristics. The LST dataset provides the dependent variable for analyzing the thermal responses of different LCZ classes. Finally, Pearson correlation analysis was employed to examine the linear associations between morphological indices and LST. Building on this analysis, XGBoost was used to build regression models, and SHAP was used to interpret the regression results.

2.3 Data Sources and Processing

2.3.1 LCZ Map

The LCZ classification framework was proposed in 2012 by Iain D. Stewart and Timothy Richard Oke, with the aim of providing a refined categorization of urban morphology to reflect the influence of different spatial forms on the microclimate[9]. The LCZ framework divides urban land into 17 categories (Tables 1, 2)—10 artificial-surface classes and 7 natural-surface classes. Since its introduction,

Table 1: Artificial-surface LCZ classes and their characteristic descriptions

LCZ class	Class name	Schematic	Building form and vegetation characteristics (B)	Surface characteristics (C)	Predominant materials (M)
LCZ 1	Compact high-rise		Dense mix of tall buildings; few or no trees	Mostly paved	Concrete, steel, stone, and glass
LCZ 2	Compact mid-rise		Dense mix of mid-rise buildings; few or no trees	Mostly paved	Stone, brick, tile, and concrete

(Continued)

Table 1: Artificial-surface LCZ classes and their characteristic descriptions (Continued)

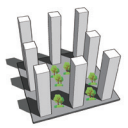
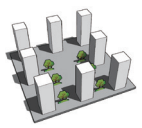
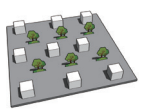
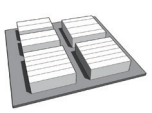
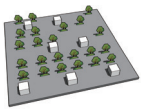
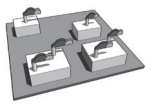
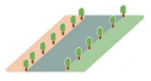
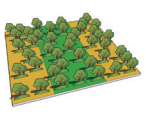
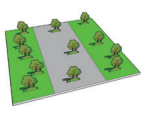
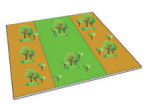
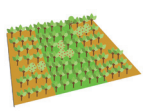
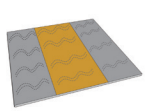
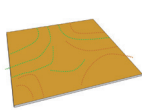
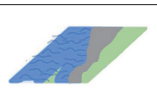
LCZ class	Class name	Schematic	Building form and vegetation characteristics (B)	Surface characteristics (C)	Predominant materials (M)
LCZ 3	Compact low-rise		Dense mix of low-rise buildings; few or no trees	Mostly paved	Stone, brick, tile, and concrete
LCZ 4	Open high-rise		Open arrangement of tall buildings; abundant low plants and scattered trees	—	Concrete, steel, stone, and glass
LCZ 5	Open mid-rise		Open arrangement of mid-rise buildings; abundant low plants and scattered trees	—	Concrete, steel, stone, and glass
LCZ 6	Open low-rise		Open arrangement of low-rise buildings; low plants and scattered trees	—	Wood, brick, stone, tile, and concrete
LCZ 7	Lightweight low-rise		Dense mix of one-story buildings	Mostly hard-packed	Wood, thatch, and corrugated metal
LCZ 8	Large low-rise		Open arrangement of large low-rise buildings; few or no trees	Mostly paved	Steel, concrete, metal, and stone
LCZ 9	Sparsely built		Sparse arrangement of small or medium-sized buildings in a natural setting; abundant low plants and scattered trees	—	—
LCZ 10	Heavy industry		Low- or mid-rise industrial structures; few or no trees	Mostly paved or hard-packed	Metal, steel, and concrete
LCZ 11	Road or street		Street or road; few or no trees	Mostly paved or hard-packed	Asphalt, concrete, brick, and stone

Table 2: Natural-surface LCZ classes and their characteristic descriptions

LCZ class	Class name	Schematic	Landscape and vegetation characteristics (V)	Surface characteristics (C)	Typical function or land-use context (F)
LCZ A	Dense trees		Heavily wooded landscape	Mostly pervious, with low plants	Natural forest, tree cultivation, or urban park
LCZ B	Scattered trees		Lightly wooded landscape	Mostly pervious, with low plants	Natural forest, tree cultivation, or urban park

(Continued)

Table 2: Natural-surface LCZ classes and their characteristic descriptions (Continued)

LCZ class	Class name	Schematic	Landscape and vegetation characteristics (V)	Surface characteristics (C)	Typical function or land-use context (F)
LCZ C	Bush, scrub		Open bushes, shrubs, and short woody vegetation	Mostly bare soil or sand	Natural scrubland or agriculture
LCZ D	Low plants		Landscape of grass, herbaceous plants, or crops; few or no trees	—	Natural grassland, agriculture, or urban park
LCZ E	Bare rock or paved		Landscape of rock or paved cover; few or no trees or plants	Rock or paved surface	—
LCZ F	Bare soil or sand		Landscape of soil or sand cover; few or no trees or plants	Soil or sand	Natural desert or agriculture
LCZ G	Water		Large or small water bodies, including seas, lakes, rivers, reservoirs, and lagoons	—	—
LCZ H	Marsh		Junction of water and shore, or marsh landscape	Water-saturated soil and sand	—
LCZ I	Farmland		Agricultural landscape	Crops or agricultural greenhouses	Farmland

the LCZ classification method has been widely applied in urban climate research. Based on our previous research, LCZs can be identified in greater detail at a spatial resolution of 2 m[29]. For the classification applied in this study, three additional LCZ types (i.e., roads, marsh, and farmland) were included[29].

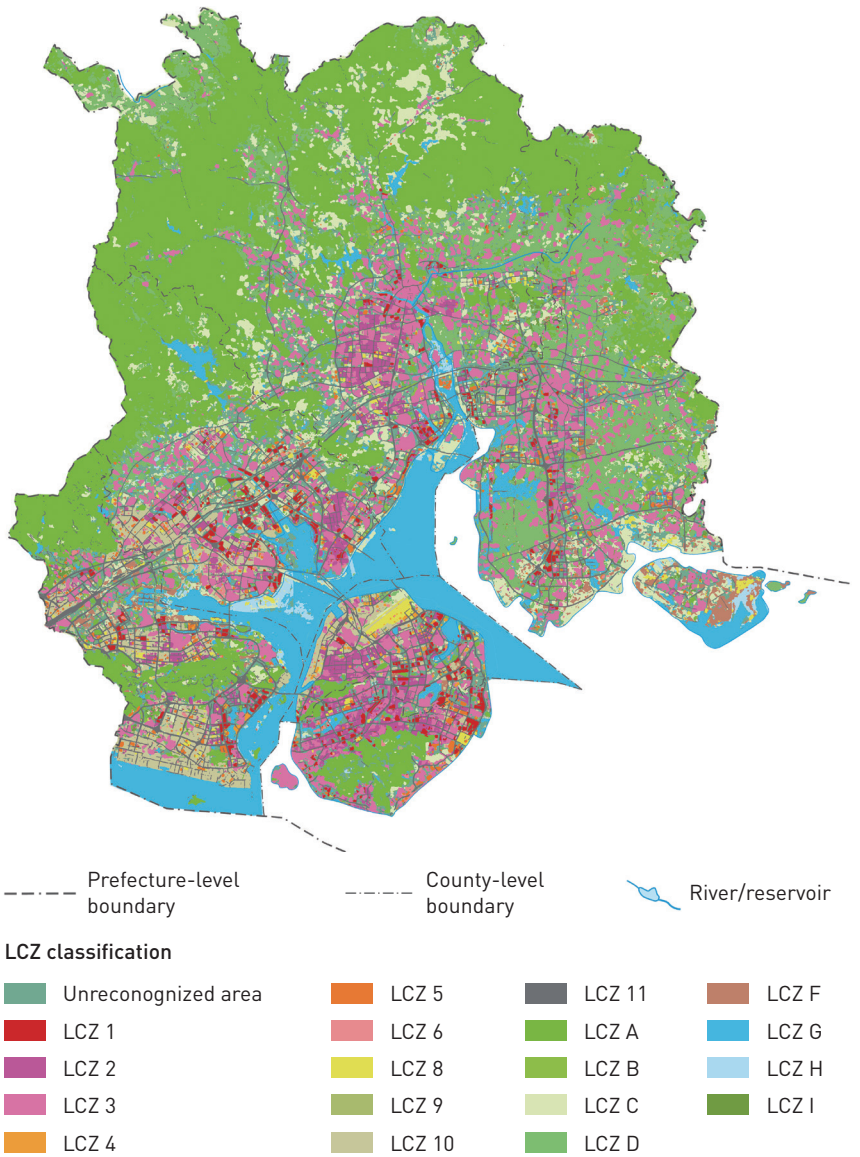
Following the LCZ classification framework, this study performed LCZ classification of Xiamen City using Google Earth imagery with a 2 m spatial resolution (Fig. 1)[29]. Administrative boundaries of Xiamen were obtained from the standard map No. Min S (2025) 202. The boundaries of LCZ patches were used as the basic sampling units for spatial morphological indices, and the patch area index was calculated. The LCZ map shows that the artificial-surface LCZs are mainly distributed along the southeastern coastal areas, while the natural-surface LCZs are predominantly located in the higher-elevation regions of the northwest, which is consistent with the urban development pattern of Xiamen.

2.3.2 LST Retrieval

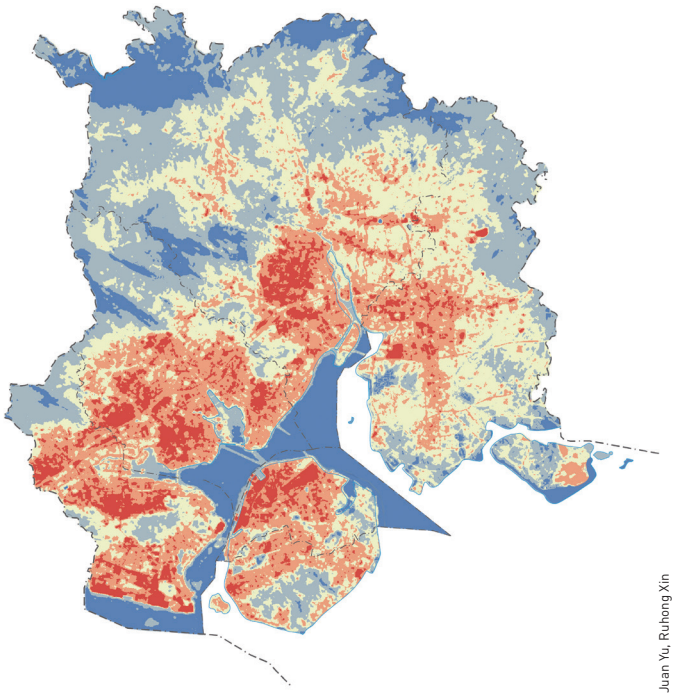
This study utilized the infrared band of Landsat 9 (LC09_L1TP_119043_20220517_20230416_02_T1) imagery for LST retrieval (Fig. 2). Because no cloud-free Landsat 9 imagery was available during the target summer period in 2022, the nearest cloud-free scene on May 17, 2022 was used to retrieve LST. This choice ensured the closest possible temporal match between the LCZ and LST datasets. According to the results, LST ranged from 0.01 °C to 52.16 °C. Areas with higher LST values were mainly concentrated along the southeastern coastal zone, whereas lower LST values were predominantly observed in the northwestern inland regions.

2.3.3 Spatial Morphology Indices

For the 10 spatial morphological indices (Table 3, Fig. 3)[30–32], this study mainly relied on building vector data, Landsat remote sensing data, and population grid data. In addition, Landsat 9 imagery was classified using a support vector machine classifier in



© Xiang Liu, Hongfei Yu, Xiaowei Lu, Juan Yu, Ruhong Xin



© Xiang Liu, Hongfei Yu, Xiaowei Lu, Juan Yu, Ruhong Xin

Fig. 1 2022 LCZ Map of Xiamen, where LCZs 7 and E were not identified.
Fig. 2 2022 LST map of Xiamen.

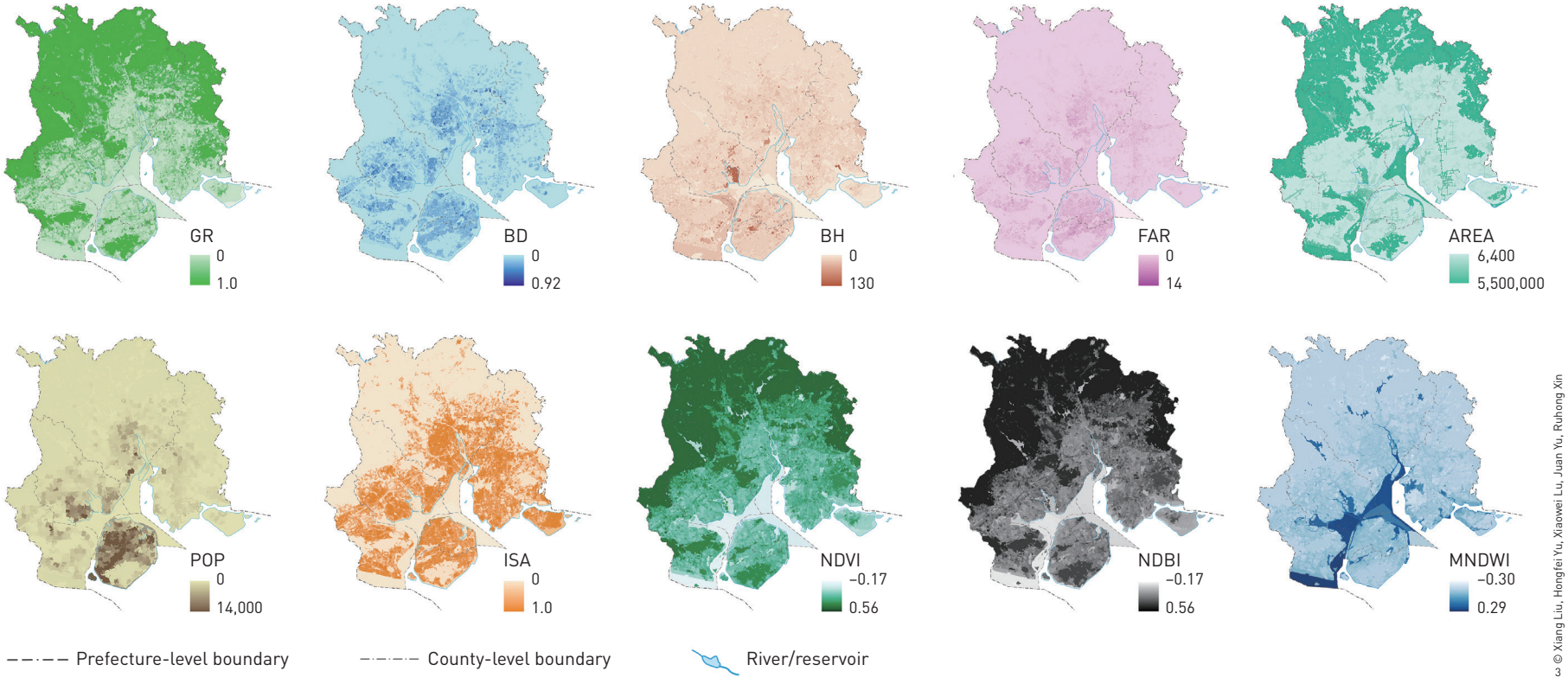
Table 3: Spatial morphological indices of LCZs

Morphological index	Year	Format	Resolution	Data source	Processing
Greening ratio (GR)	2022	Raster	30 m	Landsat 9 imagery, U.S. Geological Survey	Derived from supervised land-cover classification and calculated within each LCZ patch
Building density (BD)	2022	Vector	—	Baidu Maps	Calculated from building footprints within each LCZ patch
Building height (BH)	2022	Vector	—	Baidu Maps	Average building-height values summarized within each LCZ patch
Floor area ratio (FAR)	2022	Vector	—	Baidu Maps	Calculated from building data within each LCZ patch
Patch area (AREA)	2022	Vector	—	LCZ dataset derived from Ref. [29]	Calculated directly from the boundary of each LCZ patch
Population (POP)	2022	Raster	100 m	WorldPop	Population-grid values summarized within each LCZ patch

(Continued)

Table 3: Spatial morphological indices of LCZs (Continued)

Morphological index	Year	Format	Resolution	Data source	Processing
Impervious surface area (ISA)	2022	Raster	30 m	Landsat 9 imagery, U.S. Geological Survey	Derived from supervised land-cover classification and calculated within each LCZ patch
Normalized difference vegetation index (NDVI)	2022	Raster	30 m	Landsat 9 imagery, U.S. Geological Survey	Calculated from Landsat 9 imagery and averaged within each LCZ patch
Normalized difference built-up index (NDBI)	2022	Raster	30 m	Landsat 9 imagery, U.S. Geological Survey	Calculated from Landsat 9 imagery and averaged within each LCZ patch
Modified normalized difference water index (MNDWI)	2022	Raster	30 m	Landsat 9 imagery, U.S. Geological Survey	Calculated from Landsat 9 imagery and averaged within each LCZ patch



© Xiang Liu, Hongfei Yu, Xiaowei Lu, Juan Yu, Ruhong Xin

Fig. 3 Calculation results of the spatial morphology indices.

ENVI 5.6 to derive the greening ratio and impervious surface area (Fig. 4). The sample pair separation values were 1.98 for building–soil, 1.99 for plant–building, 1.99 for building–water, 1.99 for plant–water, 2.00 for plant–soil, and 2.00 for water–soil. All datasets were projected into the WGS 1984 UTM Zone 50N coordinate system. The boundaries of the LCZ patches were used as the basic calculation units. Raster-based variables were extracted in ArcGIS Pro 3.6 using the Zonal Statistics as Table tool, with the mean value used as the summary statistic.

2.4 Statistical and Machine-Learning Methods

2.4.1 Pearson Correlation Analysis

Pearson correlation analysis, based on statistical principles, measures the degree of linear association between two variables

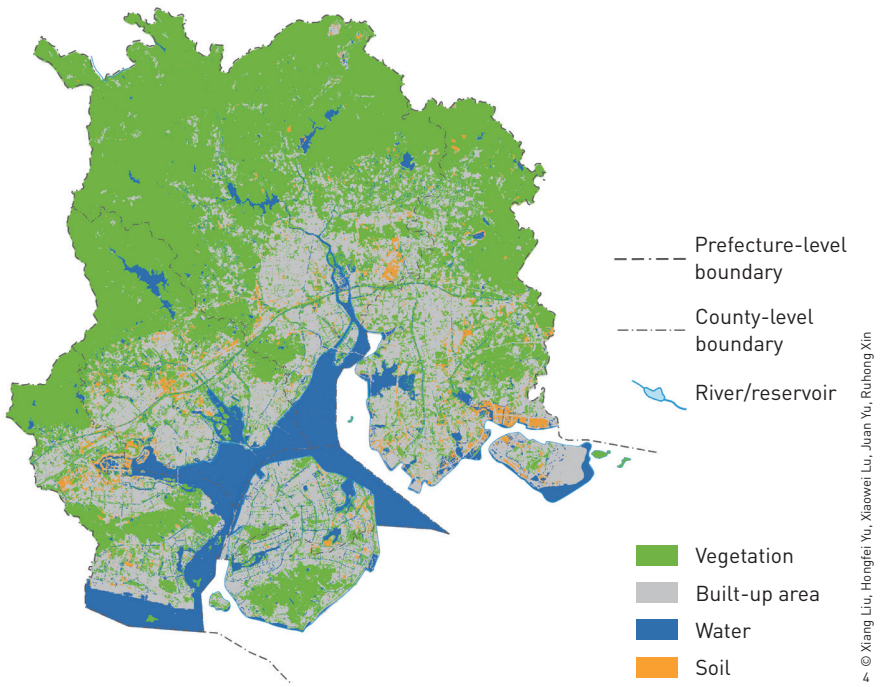


Fig. 4 Supervised land use classification of Xiamen.

by calculating the ratio of their covariance to the product of their standard deviations. This coefficient eliminates the influence of units and magnitude, thereby allowing correlations across different problems to be compared[33]:

$$r = \frac{\sum_{i=1}^{n}(x_i-\bar{x})(y_i-\bar{y})}{\sqrt{\sum_{i=1}^{n}(x_i-\bar{x})^2}\sqrt{\sum_{i=1}^{n}(y_i-\bar{y})^2}}, \quad (1)$$

where x_i and y_i represent the values of the two variables for the i-th sample, $\bar{x}$ and $\bar{y}$ are the mean values of the two variables. The correlation coefficient (r) ranges from –1 to 1, where values close to 1 indicate a strong positive correlation, values close to –1 indicate a strong negative correlation, and values near 0 suggest no linear relationship.

2.4.2 XGBoost and SHAP Analyses

Pearson correlation analysis provides a straightforward first-order assessment of the bivariate linear associations between individual urban morphological indicators and LST, thereby offering an initial indication of the direction and magnitude of potential effects. However, because Pearson's r is inherently pairwise and linear, it cannot disentangle the relative importance of predictors when multiple, potentially collinear indicators act simultaneously, capture nonlinear responses and threshold effects that are common in urban thermal processes, or quantify synergistic or interactive effects among indicators (i.e., whether the contribution of one feature depends on the level of another)[31]. To address these limitations and to obtain a more robust, multivariate, and mechanism-informative interpretation, an XGBoost model was further employed to learn the potentially nonlinear and interactive mapping from urban morphology to LST. SHapley Additive exPlanations (SHAP) was then applied to decompose the model predictions into feature-wise contributions, enabling both global importance ranking and local, instance-level explanation, as well as the exploration of feature interactions through dependence patterns[34].

XGBoost is an optimized machine-learning algorithm that integrates key merits of both linear models and tree-based methods. Built on the Gradient Boosting Decision Tree (GBDT) framework, it constructs a strong learner by sequentially aggregating multiple weak learners under the boosting paradigm. Each weak learner corresponds to a regression tree, and trees are added in a stage-wise manner by iteratively fitting the negative gradient of the loss function (i.e., gradient descent in function space). The final prediction is obtained as the additive sum of the outputs from all trees[35]. The model can be expressed as follows:

$$\hat{y}_i = \sum_{i=1}^{t} f_t(x_i), \quad (2)$$

where $\hat{y}_i$ denotes the predicted LST value, x_i represents the explanatory variables; t is the number of trees; and f_t denotes the CART function learned by t-th tree.

SHAP is a post hoc interpretability framework for explaining model outputs, originally derived from cooperative game theory. It treats each feature as a "contributor" to the prediction and quantifies the average change in the model output when a given feature is present versus absent across all possible feature coalitions. By computing a contribution value for each feature, SHAP measures the marginal effect of that feature on the prediction and provides an additive explanation for otherwise black-box machine-learning models. The SHAP value represents the contribution of a feature variable to the model's predicted output and is defined as follows[36]:

$$\phi_P = \sum_{S\subseteq\{x_1,\ldots,x_p\}/\{x_p\}} \frac{|S|!(P-|S|-1)!}{P!}\left(f(S\cup\{x_p\}) - f(S)\right), \quad (3)$$

where ϕ_p denotes the SHAP value of the p-th feature; p is the index of the feature being explained, whereas P is the total number of input features; x_p represents the p-th feature; S denotes any subset of the complete feature set that does not contain x_p; and $|S|$ is the number of features included in S. The $f(S)$ represents the model output based on the feature coalition S, while $f(S \cup \{x_p\})$ represents the model output after adding feature x_p to S. Therefore, $f(S \cup \{x_p\}) - f(S)$ denotes the

marginal contribution of feature x_p to the model prediction under the feature coalition S. The weighting term accounts for all possible orders in which the feature may enter the model.

3 Results and Analysis

3.1 Correlations Between LCZ Spatial Morphological Indices and LST

This study calculated the correlations between spatial morphological indices and LST using the Pearson correlation coefficient. The results show that the indices passing the significance test exhibit distinct differentiation across different LCZs. Overall, the correlations between morphological indices and LST vary significantly among LCZ patches (Fig. 5).

Using the natural breaks method, the correlation coefficients of the 10 indices with LST were categorized into three groups: high, moderate, and low. The indices with the high correlations were ISA, BD, FAR, NDBI, MNDWI and NDVI. Their correlations with LST in LCZs were significantly higher than those of other indices, with mean absolute correlation coefficients of 0.40, 0.37, 0.34, 0.30, 0.27, and 0.25, respectively. This indicates that within LCZ patches, these six indices exert the greatest influence on LST. The indices with moderate correlations were BH, GR, and POP, with correlation coefficients of 0.25, 0.24, and 0.24, respectively. The index with the lowest correlation was AREA, with a mean absolute correlation value of 0.09.

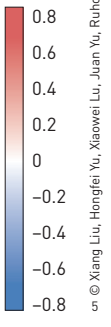
Building-related indices can be adjusted through planning and design interventions during urban development. Therefore, optimizing these indices represents a key strategy for improving the urban thermal environment. Among the indices related to building conditions (i.e., BD, BH, FAR), BD exhibited the strongest correlation with LST, with a mean absolute coefficient of 0.37. Furthermore, the correlation between BD and LST was statistically significant across all LCZ classes except LCZ 4. FAR exhibited the second-strongest correlation with LST, with a mean absolute correlation coefficient of 0.34.

3.2 Feature Importance of Morphological Indices

The XGBoost regression results show that the coefficient of determination (R^2) between the spatial morphology indices and LST ranges from 0.12 to 0.78 across different LCZs, indicating pronounced LCZ-specific differences in how spatial morphology influences LST (Fig. 6). Among the artificial-surface LCZs, LCZ 10 and LCZ 11 exhibit the highest explanatory power (R^2 = 0.65), followed by LCZ 3 (R^2 = 0.52), whereas LCZ 6 shows the lowest R^2 (0.12). For natural-surface LCZs, LCZ G achieves the highest R^2 (0.78), followed by LCZ A (R^2 = 0.57), while LCZ C records the lowest R^2 (0.19).

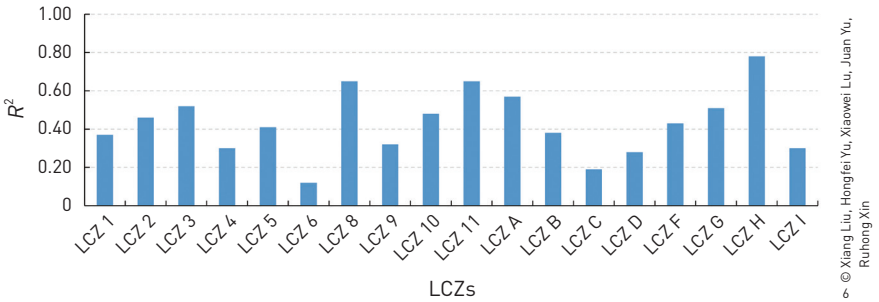
In Fig. 7, the feature-importance ranking of the 10 spatial morphology indices shows pronounced LCZ-dependent heterogeneity in the dominant controls on LST. For compact built LCZs, indicators related to surface imperviousness and built-up intensity consistently rank highest: for example, LCZ 1 is primarily driven by ISA and POP, while LCZ 2 is dominated by NDBI and BD, indicating that anthropogenic surface sealing and compactness are key determinants of thermal variability in these urban fabrics. In heavy-industry and road-related LCZs, the model places particularly strong weight on imperviousness and development intensity, e.g., LCZ 10 is led by ISA, followed by POP, NDBI, FAR, and BD, suggesting that heat accumulation is tightly coupled with high-intensity built form. By contrast, LCZ 4 exhibits a distinct importance structure in

	GR	BD	BH	FAR	AREA	POP	ISA	NDVI	NDBI	MNDWI
LCZ 1	−0.24**	0.24**	0.03	−0.16**	−0.07*	0.11**	0.43**	−0.07*	0.32**	−0.29**
LCZ 2	−0.32**	0.52**	0.08**	0.37**	0.10**	0.06*	0.44**	−0.34**	0.51**	−0.10**
LCZ 3	−0.43**	0.52**	0.26**	0.46**	0.11**	0.29**	0.52**	−0.52**	0.47**	0.32
LCZ 4	−0.31	0.48	0.28	0.56**	0.16	−0.07	0.43	−0.08	0.46	−0.49
LCZ 5	−0.33**	0.42**	0.22**	0.39**	0.03	0.19**	0.48**	−0.26**	0.43**	−0.11**
LCZ 6	−0.17*	0.39**	0.22**	0.41	−0.12	0.35**	0.33**	−0.05	0.22**	−0.18**
LCZ 8	−0.17**	0.50**	0.42**	0.45**	−0.15**	0.25**	0.55**	0.14**	0.36**	−0.49**
LCZ 9	−0.08*	0.35**	0.33**	0.36**	0.13**	0.20**	0.43**	0.14**	0.08*	−0.33**
LCZ 10	−0.31**	0.54**	0.36**	0.51**	0.01**	0.23**	0.57**	−0.19**	0.46**	−0.26**
LCZ 11	−0.41**	0.46**	0.35**	0.37**	0.06**	0.22**	0.58**	−0.22**	0.40**	−0.14**
LCZ A	0.40**	0.22**	0.26**	0.21**	−0.04	0.15**	0.19**	0.55**	−0.25**	−0.63**
LCZ B	0.00	0.21*	0.07	0.20*	0.01	0.36**	0.28**	0.17	0.05	−0.35**
LCZ C	−0.27**	0.22**	0.19**	0.20**	0.03	0.36**	0.33**	−0.25**	0.37**	−0.04
LCZ D	−0.17**	0.16**	0.21**	0.17**	0.03	0.34**	0.20**	−0.17**	0.20**	0.01
LCZ F	−0.05	0.31**	0.30**	0.30**	−0.10**	0.24**	0.24**	0.12**	0.11**	−0.32**
LCZ G	0.31**	0.32**	0.20**	0.26**	−0.19**	0.17**	0.27**	0.49**	−0.24**	−0.54**
LCZ H	0.28**	0.43**	0.46**	0.37**	−0.14	0.41**	0.60**	0.61**	0.00	−0.71**
LCZ I	−0.22**	0.45**	0.18**	0.39**	−0.05**	0.40**	0.24**	−0.21**	0.33**	−0.13**



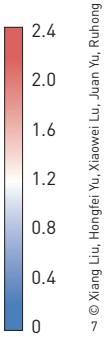
© Xiang Liu, Hongfei Yu, Xiaowei Lu, Juan Yu, Ruhong Xin

Fig. 5 Correlations between LCZ spatial morphological indices and LST (* indicates $p < 0.05$, ** indicates $p < 0.01$; two-tailed).



© Xiang Liu, Hongfei Yu, Xiaowei Lu, Juan Yu, Ruhong Xin

LCZ 1	ISA: 0.51	POP: 0.44	NDBI: 0.34	GR: 0.20	BH: 0.15	NDVI: 0.14	BD: 0.13	AREA: 0.11	MNDWI: 0.11	FAR: 0.10
LCZ 2	NDBI: 0.88	BD: 0.57	POP: 0.52	NDVI: 0.27	GR: 0.17	MNDWI: 0.17	FAR: 0.15	ISA: 0.14	AREA: 0.12	BH: 0.07
LCZ 3	POP: 0.79	NDVI: 0.42	FAR: 0.29	GR: 0.28	MNDWI: 0.20	ISA: 0.19	AREA: 0.14	BD: 0.14	NDBI: 0.11	BH: 0.07
LCZ 4	MNDWI: 0.87	FAR: 0.72	AREA: 0.41	POP: 0.32	BH: 0.15	NDBI: 0.10	NDVI: 0.10	BD: 0.04	ISA: 0.03	GR: 0.00
LCZ 5	POP: 0.72	ISA: 0.62	NDBI: 0.40	FAR: 0.24	NDVI: 0.19	BD: 0.19	GR: 0.18	MNDWI: 0.17	BH: 0.13	AREA: 0.07
LCZ 6	POP: 1.16	ISA: 0.58	MNDWI: 0.30	NDBI: 0.24	AREA: 0.20	GR: 0.15	FAR: 0.14	NDVI: 0.13	BH: 0.11	BD: 0.10
LCZ 8	BD: 0.99	POP: 0.85	NDBI: 0.77	MNDWI: 0.57	NDVI: 0.49	ISA: 0.38	FAR: 0.37	GR: 0.19	BH: 0.17	AREA: 0.11
LCZ 9	POP: 0.73	MNDWI: 0.46	GR: 0.28	FAR: 0.27	NDVI: 0.22	AREA: 0.22	ISA: 0.20	BH: 0.15	NDBI: 0.10	BD: 0.08
LCZ 10	ISA: 1.12	POP: 0.78	NDBI: 0.69	FAR: 0.63	BD: 0.60	BH: 0.25	GR: 0.25	MNDWI: 0.22	AREA: 0.21	NDVI: 0.19
LCZ 11	POP: 1.22	ISA: 0.65	FAR: 0.30	NDBI: 0.30	NDVI: 0.30	MNDWI: 0.25	BH: 0.13	GR: 0.11	AREA: 0.09	BD: 0.05
LCZ A	MNDWI: 0.68	POP: 0.54	NDVI: 0.32	AREA: 0.19	NDBI: 0.16	ISA: 0.14	FAR: 0.13	GR: 0.13	BD: 0.08	BH: 0.05
LCZ B	POP: 0.83	ISA: 0.18	GR: 0.17	NDVI: 0.17	NDBI: 0.15	AREA: 0.11	BH: 0.08	MNDWI: 0.08	FAR: 0.06	BD: 0.01
LCZ C	POP: 1.08	NDBI: 0.56	GR: 0.22	MNDWI: 0.18	ISA: 0.18	NDVI: 0.15	FAR: 0.13	AREA: 0.12	BH: 0.08	BD: 0.03
LCZ D	POP: 0.85	GR: 0.27	NDBI: 0.20	AREA: 0.18	ISA: 0.15	NDVI: 0.13	MNDWI: 0.13	FAR: 0.08	BH: 0.04	BD: 0.03
LCZ F	POP: 0.69	MNDWI: 0.36	NDBI: 0.29	FAR: 0.24	GR: 0.18	BD: 0.16	NDVI: 0.15	ISA: 0.13	AREA: 0.12	BH: 0.06
LCZ G	POP: 0.94	MNDWI: 0.50	NDVI: 0.39	AREA: 0.22	ISA: 0.17	FAR: 0.16	GR: 0.12	BD: 0.12	NDBI: 0.10	BH: 0.03
LCZ H	NDVI: 2.33	NDBI: 0.69	POP: 0.47	ISA: 0.33	AREA: 0.27	MNDWI: 0.19	BH: 0.15	GR: 0.10	FAR: 0.09	BD: 0.02
LCZ I	POP: 0.47	NDBI: 0.34	FAR: 0.23	ISA: 0.20	NDVI: 0.17	MNDWI: 0.16	BD: 0.14	GR: 0.10	AREA: 0.07	BH: 0.05



© Xiang Liu, Hongfei Yu, Xiaowei Lu, Juan Yu, Ruhong Xin

Fig. 6 Explanatory power (R^2) of the XGBoost models across LCZs.
Fig. 7 XGBoost feature-importance ranking.

which MNDWI and FAR outweigh most other predictors, and GR contributes minimally, highlighting that moisture-related surface conditions and vertical intensity can dominate in specific open/high-rise contexts. For natural-surface LCZs, vegetation- and water-sensitive indices become more prominent, e.g., MNDWI ranks first in LCZ A, and NDVI overwhelmingly dominates LCZ H, reflecting a shift from anthropogenic controls to biophysical regulation. Overall, these LCZ-specific importance profiles confirm that the key predictors of LST differ substantially by LCZ class, supporting the necessity of differentiated, class-sensitive heat-mitigation strategies.

3.3 SHAP Dependence Cross-Analysis of Morphological Indices

Given the large number of dependence plots, presenting all LCZ dependence plots would be impractical. Therefore, LCZ 2 was selected as a representative example to illustrate the inter-feature dependence relationships. The SHAP dependence plots (Fig. 8) are used to unpack nonlinear marginal effects and pairwise interactions captured by the XGBoost model. In each panel, the x-axis shows the raw feature value, the y-axis shows its SHAP contribution to the predicted LST, and point color encodes the interacting feature specified in the plot. Overall, the patterns are clearly non-monotonic for several predictors, indicating that the model response is characterized by thresholds and saturation rather than simple linear sensitivities.

Across the SHAP dependence plots, three recurring response patterns can be identified. We take the three indices—BD, NDVI, and GR—as examples, as their trends are highly representative. First, a threshold-type amplification can be observed in FAR–NDBI, BH–NDBI, BD–MNDWI, and POP–NDBI relationships in Fig. 8. Taking BD–MNDWI as an example, with MNDWI represented by point color. The SHAP contribution of BD remains small or slightly negative at low BD values but increases sharply beyond an intermediate range, indicating a pronounced warming contribution once building density exceeds a certain threshold. The color distribution shows that samples with high BD and large positive SHAP values tend to coincide with relatively higher MNDWI values, suggesting that the BD response may vary across different MNDWI conditions. Second, a nonlinear cooling pattern can be observed in AREA–BD, ISA–MNDWI, and NDVI–MNDWI relationships in Fig. 8. Taking NDVI–MNDWI as an example , with MNDWI represented by point color. As NDVI increases, its SHAP values show an overall tendency toward more negative values, and the strongest cooling contributions are

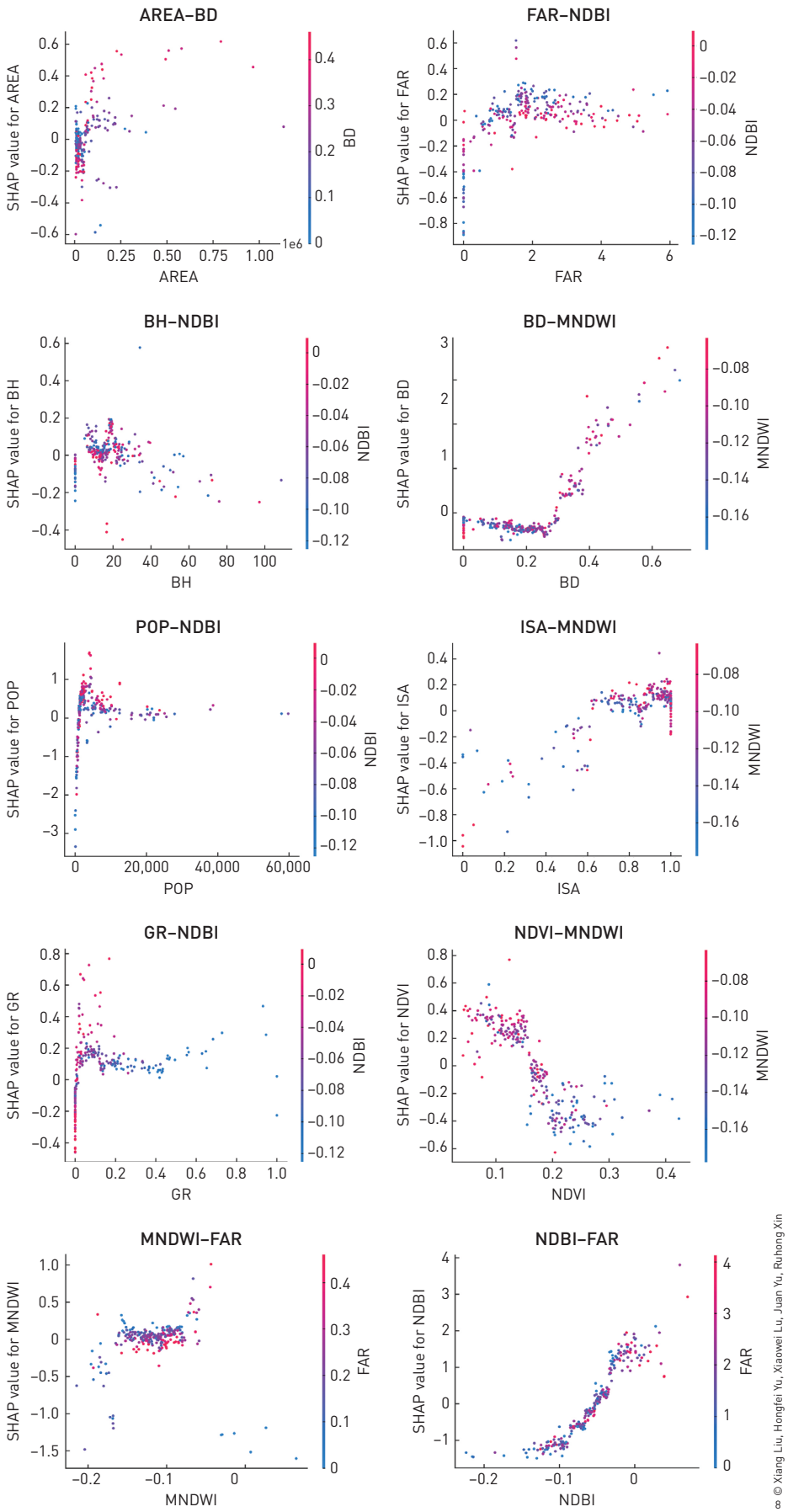


Fig. 8 SHAP dependence cross-analysis of indices.

concentrated at higher NDVI values, indicating that additional vegetation may generate stronger cooling beyond a certain threshold. The color distribution further indicates that this cooling response varies with MNDWI rather than remaining uniform across different contexts. Third, a diminishing-return pattern can be observed in MNDWI–FAR, GR–NDBI, and NDBI–FAR relationships in Fig. 8. Taking GR–NDBI as an example, with NDBI represented by point color. When NDBI is greater than –0.06, increasing GR substantially increases SHAP value, whereas the response gradually levels off when GR is greater than 0.2. This suggests that the marginal cooling benefit weakens once greening exceeds a certain level.

4 Discussion

4.1 Research Contributions

First, at the conceptual level, this study advances LCZ-based thermal environment research from a single-factor or class-comparison perspective toward a multidimensional morphology–temperature coupling perspective at the LCZ patch scale. Building on the LCZ framework[9], the study jointly examines building-form, biophysical, and patch attributes, rather than interpreting LST variation through isolated indicators. This helps address a common limitation in previous urban heat studies, namely insufficient characterization of the combined and heterogeneous effects of urban morphology on thermal responses across local spatial units[19,35]. In this sense, the study strengthens the explanatory capacity of LCZ research for high-density coastal cities and provides a more operational basis for differentiated urban heat mitigation.

Second, at the methodological level, this study develops a progressive and interpretable analytical workflow that integrates Pearson correlation, XGBoost, and SHAP. The workflow moves from linear screening to nonlinear modeling and then to mechanism-oriented interpretation, thereby improving robustness relative to correlation-only or conventional regression approaches. XGBoost is well suited for capturing nonlinearities and interactions among multiple predictors[35], while SHAP provides additive, feature-level explanations for both global importance and local contribution patterns[34,36]. This combination allows the study not only to estimate the explanatory power of spatial morphology for LST, but also to identify threshold effects, directionality, and interaction structures that are directly relevant to planning decisions.

Third, at the empirical and planning-application level, the Xiamen case provides evidence for prioritized and class-sensitive

© Xiang Liu, Hongfei Yu, Xiaowei Lu, Juan Yu, Ruhong Xin

thermal governance. The results identify ISA, BD, FAR, NDBI, NDVI, and MNDWI as the most influential indicators, while the XGBoost–SHAP analysis further reveals three recurring interaction patterns: threshold-type amplification, nonlinear cooling, and diminishing-return effects. These findings move beyond generic "increase greening" recommendations by indicating that the thermal benefits of morphological regulation are conditional, nonlinear, and LCZ-context dependent, thus offering a more precise basis for climate-adaptive urban design and spatial optimization.

4.2 Heterogeneous Effects of Spatial Morphology on LST in LCZs

The results of this study demonstrate that spatial morphology exerts significantly heterogeneous effects on LST in LCZs. This pattern may be attributed to the complexity and heterogeneity of urban space, whereby the influence of morphological factors on LST varies substantially across different urban areas and LCZ patches[37–38]. For example, the results of a study of urban form and LST within Beijing's Fifth Ring Road found that the effects of morphological indicators (e.g., BD, FAR, GR) on LST exhibited spatial non-stationarity, with considerable differences across regions[39]. Similarly, a study of FAR and mean LST in Tianjin's central urban area reported a bidirectional effect of FAR[40]. These findings underscore that the impacts of urban spatial morphology on LST are characterized by pronounced type-specific and spatial heterogeneity[41–42]. Therefore, when optimizing the urban thermal environment, such heterogeneity must be carefully considered to avoid ineffective or counterproductive cooling strategies.

From a planning practice perspective, the heterogeneity identified in this study can be translated into LCZ-specific intervention guidelines rather than one-size-fits-all cooling measures. Specifically, planners may use LCZ patches as operational units to build a "diagnosis–intervention–priority" matrix: in LCZs dominated by high ISA/NDBI/BD effects, priority should be given to impervious-surface reduction, street shading, material albedo optimization, and ventilation-oriented block renewal; in LCZs where NDVI/GR/MNDWI show stronger cooling contributions, strategies should focus on blue–green space allocation, ecological corridor continuity, and water-sensitive landscape retrofits. The threshold and diminishing-return patterns revealed by SHAP further imply that intervention intensity should be calibrated by local conditions to avoid overinvestment with limited thermal benefit. In this sense, the LCZ–XGBoost–SHAP framework can support scenario-based planning and phased renewal by ranking candidate measures according to expected cooling gains, implementation feasibility, and co-benefits such as stormwater regulation and ecological improvement[10,23–24].

4.3 LCZ Framework for Optimizing Urban Thermal Environments

Traditional urban land-use classification approaches exhibit two main limitations when addressing urban thermal environment issues. First, their classification systems are relatively coarse and contain only a few categories, focusing primarily on indicators such as density and land-use function[23,40]. For instance, conventional classifications often divide urban land into broad categories such as commercial, residential, and industrial zones. Such simplified delineations neglect the complex microclimatic factors within each zone, including BH, BD, GR, and FAR, all of which influence the urban thermal environment and interact with each other. Second, traditional land-use classifications rarely incorporate 3D spatial information, despite the fact that these vertical morphological features exert significant impacts on urban climate. For example, BH strongly affects shading patterns[43], wind flow[44], and heat diffusion[45], thereby shaping local thermal conditions.

By contrast, the LCZ framework effectively overcomes these limitations. Firstly, LCZ classification dissects the spatial characteristics of localized urban areas by explicitly accounting for key factors such as building morphology, surface materials, and vegetation cover, thereby providing a precise delineation of each unique LCZ patch. Secondly, LCZs possess dynamic adaptability: as urban development progresses, the classification can be updated in near real time, allowing flexible adjustments to reflect changing conditions. Taken together, these advantages highlight that LCZ-based research provides a robust foundation for the precise optimization of urban thermal environments. Thirdly, LCZs can be operationalized as a spatial decision layer by coupling LCZ patches with corridor-network tools (e.g., Linkage Mapper) and airflow simulation for ventilation path optimization, and with multi-objective land-use and blue–green allocation models to jointly optimize cooling gains, stormwater regulation, and development constraints under scenario-based planning and phased regeneration implementation[23–24,44].

5 Conclusions and Prospects

This study examined the relationships between 10 morphological indices and LST in LCZs. Correlation analysis was applied to assess whether these indices exert significant effects on LST. Based on the correlation analysis, XGBoost models were constructed to analyze the explanatory power of spatial indices for LST across different LCZs. Furthermore, SHAP was applied to capture the interactions among indices. The main results are as follows:

The results demonstrate that the thermal effects of urban spatial

morphology are strongly LCZ-dependent. ISA, BD, FAR, NDBI, NDVI, and MNDWI emerged as the most influential indicators, while the explanatory power of the XGBoost models varied substantially across LCZ classes, with R^2 values ranging from 0.12 to 0.78. SHAP analysis further revealed that the effects and interactions of morphological indicators were predominantly characterized by threshold amplification, nonlinear cooling, and diminishing returns, highlighting the nonlinear and context-specific nature of morphology–LST relationships.

This study established a replicable analytical workflow for examining the thermal effects of urban spatial morphology within the LCZ framework in a high-density coastal city. By integrating a high-resolution LCZ map with Landsat-derived LST and 10 spatial morphological indices, and by combining correlation analysis, XGBoost regression, and SHAP interpretation, the study moved beyond single-factor linear description toward a more systematic identification of nonlinear and interactive mechanisms. The results not only confirmed the joint explanatory capacity of multidimensional morphology for LCZ thermal variation, but also revealed interpretable interaction patterns, thereby strengthening the scientific basis for refined thermal-environment regulation. Overall, the proposed LCZ–XGBoost–SHAP framework provides a practical and transferable methodological paradigm for climate-adaptive urban design and differentiated planning governance in coastal high-density cities.

This study is limited by the restricted range of morphological indicators and the absence of temporal comparisons. The 10 selected indices do not fully capture urban form characteristics such as sky view factor, building configuration, materials, and color, while the reliance on a single-period Landsat dataset prevents assessment of seasonal and interannual variation. Future research should therefore incorporate more comprehensive morphological variables and integrate multi-source or temporally corrected datasets to improve model explanatory power and examine the long-term temporal heterogeneity of morphology–LST relationships within different LCZs.

ELECTRONIC SUPPLEMENTARY MATERIAL

Supplementary material is available in the online version of this article at https://doi.org/10.15302/J-LAF-2026-0038.

Competing interests | The authors declare that they have no competing interests.

REFERENCES

[1] World Meteorological Organization. (2024, March 19). *State of the Global Climate 2023*.

[2] Intergovernmental Panel on Climate Change (IPCC). (2023). *Climate Change 2022—Impacts, Adaptation and Vulnerability*. Cambridge University Press.

[3] Yu, K. (2021). Climate adaptation and resilience. *Landscape Architecture Frontiers*, *9*(6), 4–7.

[4] United Nations (n.d.). *Goal 13: Climate action*.

[5] Zuo, W., Ren, Z., Shan, X., Zhou, Z., & Deng, Q. (2024). Analysis of urban heat island effect in Wuhan urban area based on prediction of urban underlying surface coverage type change. *Advances in Meteorology, 2024*, 4509221.

[6] Aizizi, Y., Kasimu, A., Liang, H., Zhang, X., Zhao, Y., & Wei, B. (2023). Evaluation of ecological space and ecological quality changes in urban agglomeration on the northern slope of the Tianshan Mountains. *Ecological Indicators*, *146*, 109896.

[7] Xiamen Municipal Bureau of Natural Resources and Planning. (2025). *Xiamen Territorial Spatial Master Planning (2021–2035)*.

[8] Cai, Z., Tang, Y., Chang, L., & Demuzere, M. (2021). Analyzing the transformation of 3d urban morphology and corresponding surface heat island effect in Beijing. *Urban Planning International*, *36*(5), 61–68.

[9] Stewart, I. D., & Oke, T. R. (2012). Local climate zones for urban temperature studies. *Bulletin of the American Meteorological Society*, *93*(12), 1879–1900.

[10] Huang, B., Qi, J., Pathak, M., Sharifi, A., Cheshmehzangi, A., Attia, S., ... He, B.-J. (2025). Climate-driven transformations: A framework for the sustainable urban landscape system to enhance heat resilience. *Sustainable Cities and Society*, *131*, 106684.

[11] Cheng, Y., & Chen, Y. (2024). Spatial and temporal characteristics of land use changes in the Yellow River Basin from 1990 to 2021 and future predictions. *Land*, *13*(9), 1510.

[12] Zhang, G., Tian, Z., Wang, Q., Sun, Y., Yang, Y., & Wang, H. (2022). Study on the influence of urban form on land surface temperature based on machine learning. *Environmental Science & Technology*, *45*, 214–227.

[13] Zhou, S., Zheng, H., Liu, X., Gao, Q., & Xie, J. (2023). Identifying the effects of vegetation on urban surface temperatures based on urban–Rural local climate zones in a subtropical metropolis. *Remote Sensing*, *15*(19), 4743.

[14] Pan, T., Li, B., & Ning, L. (2023). Impervious surface area patterns and their response to land surface temperature mechanism in urban–Rural regions of Qingdao, China. *Remote Sensing*, *15*(17), 4265.

[15] Han, W. (2023). Analyzing the scale dependent effect of urban building morphology on land surface temperature using random forest algorithm. *Scientific Reports*, *13*(1), 19312.

[16] Xiao, Y., Dai, S., & Zhao, B. (2020). Mitigation of urban heat island effect with small-scale parks—An empirical study on community parks in Nanjing, Jiangsu Province. *Landscape Architecture Frontiers*, *8*(3), 26.

[17] van der Velde, R., de Wit, S., & Pouderoijen, M. (2023). Cool tree architecture: A descriptive framework for a tree architecture typology to

temper urban microclimates. *Landscape Architecture Frontiers*, *11*(5), 30–42.

[18] Zhou, X., & Chen, H. (2018). Impact of urbanization-related land use land cover changes and urban morphology changes on the urban heat island phenomenon. *Science of the Total Environment*, *635*, 1467–1476.

[19] Yang, J., Ren, J., Sun, D., Xiao, X., Xia, J. C., Jin, C., & Li, X. (2021). Understanding land surface temperature impact factors based on local climate zones. *Sustainable Cities and Society*, *69*, 102818.

[20] Lau, K. K.-L., Chung, S. C., & Ren, C. (2019). Outdoor thermal comfort in different urban settings of sub-tropical high-density cities: An approach of adopting local climate zone (LCZ) classification. *Building and Environment*, *154*, 227–238.

[21] Parvar, Z., Mohammadzadeh, M., & Saeidi, S. (2024). LCZ framework and landscape metrics: Exploration of urban and peri-urban thermal environment emphasizing 2/3D characteristics. *Building and Environment*, *254*, 111370.

[22] Badaro-Saliba, N., Adjizian-Gerard, J., Zaarour, R., & Najjar, G. (2021). LCZ scheme for assessing urban heat island intensity in a complex urban area (Beirut, Lebanon). *Urban Climate*, *37*, 100846.

[23] Zhang, Y., Ge, J., Bai, X., & Wang, S. (2025). Blue–Green space seasonal influence on land surface temperatures across different urban functional zones: Integrating random forest and geographically weighted regression. *Journal of Environmental Management*, *374*, 123975.

[24] Liang, C., Zhang, R.-C., Zeng, J., & Shen, Z.-J. (2021). A land-use decision approach integrating thermal regulation, stormwater management, and economic benefits based on urbanization stage identification. *Science of the Total Environment*, *779*, 146415.

[25] Tang, L., Zhao, Y., Yin, K., & Zhao, J. (2013). Xiamen. *Cities*, *31*, 615–624.

[26] Jing, D. (2021). *Green Roof Planning in High-Density Urban Areas-A Case Study of Xiamen Island* [Doctoral Dissertation]. Tianjin University.

[27] Jia, W., Ren, G., Jin, F., He, J., & Zhang, P. (2023). Spatial-temporal characteristics of the urban heat island effect in Xiamen, China. *Urban Climate*, *52,* 101725.

[28] Chen, Z., Lin, X., Li, M., Chen, Y., Huang, Y., Zhu, Y., ... Dong, J. (2023). Spatio-temporal dynamic characteristics and landscape connectivity of heat islands in Xiamen in the face of rapid urbanization. *Sustainability*, *15*(19), 14603.

[29] Liu, X., Zeng, S., Namaiti, A., & Xin, R. (2023). Comparison between three convolutional neural networks for local climate zone classification using google earth images: A case study of the Fujian Delta in China. *Ecological Indicators*, *148*, 110086.

[30] Lu, H., Li, F., Yang, G., & Sun, W. (2021). Multi-scale impacts of 2D/3D urban building pattern in intra-annual thermal environment of Hangzhou, China. *International Journal of Applied Earth Observation and Geoinformation*, *104*, 102558.

[31] Bai, D., Miao, C., Xi, Y., Liu, H., & He, C. (2025). The impact of 2D/3D building morphology and green spaces on urban heat environments: Relative contributions, interaction and marginal effects. *Ecological Indicators*, *180*, 114296.

[32] Chen, L., & Guo, G. (2026). Exploring the nonlinear interactions and threshold effects of urban building morphology and green space on land surface temperature in high-density areas: A cross-city comparative study. *Sustainable Cities and Society*, *136*, 107069.

[33] Kim, H.-Y. (2018). Statistical notes for clinical researchers: Covariance and correlation. *Restorative Dentistry & Endodontics*, *43*(1), e4.

[34] Lundberg, S. M., Erion, G., Chen, H., DeGrave, A., Prutkin, J. M., Nair, B., ... Lee, S. (2020). From local explanations to global understanding with explainable AI for trees. *Nature Machine Intelligence*, *2*(1), 56–67.

[35] Chen, T., & Guestrin, C. (2016). XGBoost: A scalable tree boosting system. *KDD'16: Proceedings of the 22nd ACM SIGKDD International Conference on Knowledge Discovery and Data Mining*, 785–794.

[36] Lundberg, S. M., & Lee, S.-I. (2017). A unified approach to interpreting model predictions. *Advances in Neural Information Processing Systems*, *30*.

[37] Huang, F., Jiang, S., Zhan, W., Bechtel, B., Liu, Z., Demuzere, M., ... Xia, W. (2023). Mapping local climate zones for cities: A large review. *Remote Sensing of Environment*, *292*, 113573.

[38] Rong, F. U., Xinmei, W. U., & Bin, C. (2023). Analysis on the spatial stratified heterogeneity and driving factors differences of the urban land surface temperature: A case study of Hefei. *Ecology and Environment*, *32*(1), 110.

[39] Sun, Z. (2020). Impact of urban morphology factors on thermal environment in high density urban areas: A case of Beijing within 5th ring road. *Ecology and Environment Sciences*, *29*(10), 2020–2027.

[40] Song, X., Huang, H., Guo, J., & Xiong, M. (2021). Research on the impact of urban morphology on thermal environment in summer: A case of Tianjin central city. *Ecology and Environment Sciences*, *30*(11), 2165–2174.

[41] Wen, D., Wang, L., Cao, Q., Hong, M., Wang, H., & Bian, G. (2024). A comparative study of the effects of urban morphology on land surface temperature in Chengdu and Chongqing, China. *Scientific Reports*, *14*(1), 25130.

[42] Peng, S., Feng, Z., Liao, H., Huang, B., Peng, S., & Zhou, T. (2019). Spatial-temporal pattern of, and driving forces for, urban heat island in China. *Ecological Indicators*, *96*, 127–132.

[43] Sun, Y., Meng, D., Song, J., Hu, F., & Li, X. (2025). Study on the diurnal dynamic changes of urban thermal environment and population heat exposure risk within Beijing's fifth ring road from the perspective of local climate zones. *Ecology and Environment Sciences*, *34*(2), 279–292.

[44] Shi, Z., Yang, J., Zhang, Y., Xiao, X., & Xia, J. C. (2022). Urban ventilation corridors and spatiotemporal divergence patterns of urban heat island intensity: A local climate zone perspective. *Environmental Science and Pollution Research*, *29*, 74394–74406.

[45] Luo, Y., Zhang, Y., Yang, K., Zhou, X., & Peng, Z. (2023). Urban surface thermal runoff generation mechanism and scenario simulation. *Water Resources Research, 59*(4), e2022WR033881.

LAF | https://doi.org/10.15302/J-LAF-2026-0038
第14卷 / 第5期 / 260038 / 2026
收稿日期 | 2025-10-18　录用日期 | 2026-06-11
中图分类号 | TU984　文献标识码 | A

城市空间形态对局地气候区地表温度的影响

刘祥[1]，于洪飞[2,*]，卢小伟[3]，于娟[1]，辛儒鸿[4]

1 济南大学土木建筑学院，济南 250022
2 中建八局第一建设有限公司, 济南 250014
3 上海市政工程设计研究总院（集团）有限公司, 上海 200092
4 西南大学园艺园林学院，重庆 400715

*通信作者
地址：济南市历下区三庆世纪财富中心C座5层
邮编：250014
邮箱：yuhongfei.young@163.com

摘要

全球变暖导致极端高温事件日益频发，城市热环境持续恶化。对城市空间形态进行精准调控是优化城市热环境的有效途径。局地气候区（LCZ）为衔接城市形态与城市热环境之间的关系提供了解释框架。本文以厦门市为研究对象，采用卷积神经网络生成高分辨率LCZ地图，并选取建筑密度、容积率和绿地率等10项空间形态指标，分析其与地表温度之间的关系。研究综合运用相关性分析、XGBoost－SHAP方法开展定量分析。结果表明：1）不透水面面积、建筑密度、容积率、归一化建筑指数、归一化植被指数和改进型归一化差异水体指数与不同LCZ类型的地表温度的相关性最强；2）XGBoost回归结果显示，10项空间形态指标对地表温度的解释力在不同LCZ类型之间存在显著差异，R^2介于0.12～0.78之间；3）SHAP分析对XGBoost模型结果进行了有效解释，10项指标之间的交互作用可概括为3种模式，即阈值放大、非线性降温和边际效应递减。研究结果可为精细化城市规划与气候适应性设计提供科学依据，并有助于提升城市气候韧性。

关键词

局地气候区；城市空间形态；地表温度；空间异质性；XGBoost－SHAP

文章亮点

- 城市空间形态对不同LCZ斑块地表温度的影响具有显著异质性
- XGBoost－SHAP揭示了城市热响应的非线性响应与交互机制
- 识别出阈值放大效应、非线性降温效应和边际效益递减效应3类非线性响应模式
- 基于LCZ类型差异的热环境调控策略有助于实现精准化城市热缓解

基金项目

- 山东省软科学重点项目（编号：2026RZB0108）
- 济南大学新引进人才科研项目（科技类）（编号：XBS2510）